Scientific Reports

https://doi.org/10.1038/s41598-026-55026-6

Article in Press

A directional nanoantenna design based on a hybrid plasmonic waveguide: theoretical analysis for biosensing applications

Received: 21 April 2026

Accepted: 21 May 2026

Published online: 01 June 2026

Cite this article as: AzimBeik M., Moradi G. & Abdipour A. A directional nanoantenna design based on a hybrid plasmonic waveguide: theoretical analysis for biosensing applications. *Sci Rep* (2026). https://doi.org/10.1038/s41598-026-55026-6

Mohammad AzimBeik, Gholamreza Moradi & Abdolali Abdipour

A Directional Nanoantenna Design Based on a Hybrid Plasmonic Waveguide: Theoretical Analysis for Biosensing Applications

Mohammad AzimBeik[1], **Gholamreza Moradi**[1,*], **and Abdolali Abdipour**[1]

[1]Department of Electrical Engineering, Amirkabir University of Technology (Tehran Polytechnic), 350 Hafez Ave, Tehran, Iran, 1591634311
[*]ghmoradi@aut.ac.ir

ABSTRACT

This paper presents a novel rectangular aperture nano-antenna (RANA) design based on a hybrid plasmonic waveguide (HPW) configuration. The performance of the HPW is evaluated through theoretical analysis and compared with results from the Finite Integration Technique (FIT). The overall performance of the RANA is investigated at an operational frequency of 450 THz using both FIT and the Finite Element Method (FEM). The nano-antenna exhibits a directional radiation pattern, which is leveraged for refractive index biosensing. The biosensor's performance is characterized using a dry protein model with a refractive index ranging from 1.7 to 1.9. The sensing mechanism relies on monitoring shifts in the beam direction and variations in the power flow peak in response to changes in the refractive index of the dry protein as a material under test (MUT). The proposed biosensor achieves a sensitivity of 34.5 degrees per refractive index unit (RIU). The biosensor maintains strong performance over a 2 percent bandwidth centered at operational frequency, enhancing its detection robustness.

Introduction

Biosensors have played a significant role in detecting material properties with distinct features in recent years. Characteristics such as minimal sample volume requirements, real-time and low-time responses, quantifiable data presentation, high precision output, nano-scale physical dimensions, and error-free data processing have steered research attention toward this domain[1–3]. A major category of modern biosensors operates on the principle of surface plasmonic waves propagation. Among these, surface plasmon resonance (SPR) biosensors represent a prominent category and have found widespread application in various sensing platforms, including ring resonator biosensors, photonic crystal biosensors, and bragg-grating-embedded ring resonator structures[4–7]. SPR biosensors have demonstrated broad applicability in biomedical diagnostics, including the detection of cancer biomarkers[8,9], tuberculosis[10], malaria[11], and viral infections such as coronavirus[12,13]. In addition, SPR biosensors are particularly attractive due to their compact structure and their suitability for on-chip integration.[14,15]. These biosensors operate by monitoring variations in electric field intensity and local field enhancement within confined regions near metal-dielectric interfaces[16]. In addition to these structures, nano-antennas offer significant potential for innovative biosensor designs. Nano-antenna structures are analyzed through the framework of surface plasmon polaritons (SPP)[17–19]. Nano-antennas, which operate based on plasmonic waves, provide an alternative approach for designing circuit-compatible devices that rely on electric field enhancement[20]. In this context, biosensors based on nano-antennas play a crucial role in monitoring variations in the characteristics of the material under test (MUT), where interactions with the MUT are often manifested as changes in its refractive index. However, detecting these variations with nano-antennas poses several challenges, including issues related to detection probability, sensitivity, physical dimensions, linearity, operating frequencies, and bandwidth limitations. The ability to distinguish such variations is critical in fields such as biotechnology, medicine, and food safety[21–23].

The demand for higher sensitivity, simplified fabrication, broadband operation, and compact device size has motivated extensive research on biosensor applications, employing SPP fields to detect changes in material properties. Several studies have investigated biosensor applications based on SPP fields for detecting variations in material properties. For example, Awasthi et al. proposed a one-dimensional annular photonic crystal structure for protein concentration detection in the visible spectral region[24]. Similarly, Kumar et al. reported an $In_{0.53}Ga_{0.47}As$-SOI-FinFET biosensor for label-free protein detection, demonstrating high surface sensitivity, strong electrostatic control, and low-noise performance[25]. In the field of nano-antenna, a circular hybrid waveguide-based nano-antenna is described in[26], also targeting the 1550 nm wavelength, with a directive radiation pattern. In a related study[27], a nano-antenna based on a symmetric hybrid plasmonic waveguide is proposed, featuring both directional and bidirectional radiation patterns. Additionally, a graphene-based terahertz metamaterial absorber has been reported for tunable sensing applications on an ultra-thin SiO_2 substrate, demonstrating near-perfect multi-band absorption in the 5–10 THz range and high refractive index sensing performance enabled by tuning the graphene Fermi energy[28]. An array of bowtie nano-antenna has been specifically designed for biosensor applications[29], enhancing local plasmonic waves. Furthermore, Safaeian et al.[30] propose a plasmonic biosensor strategy that employs optical beam steering at a wavelength of 633 nm. In this work, by varying properties of the MUT, the direction of the emitted optical beam changes. A polished SPR-based photonic crystal fiber sensor coated with aluminum-doped zinc oxide has been proposed in[31], achieving ultra-wide refractive index detection (1.18–1.45) for chemical and biomedical sensing applications.

This paper proposes a radiation-pattern-based biosensor employing a rectangular aperture nano-antenna for detecting refractive index variations of dry protein as the material under test (MUT). The dry protein is modeled with a refractive index range of 1.7–1.9 at 450 THz, which is considered the sensing target. The proposed structure is developed by integrating a rectangular hybrid plasmonic waveguide (HPW) with a rectangular aperture radiating element, enabling directional far-field emission. To provide physical insight and enable systematic design, a theoretical formulation is derived to obtain the dispersion equation and the supported propagation modes of the HPW. A genetic algorithm (GA) is subsequently applied to solve the dispersion relation and identify the dominant mode with the maximum propagation length, which is then utilized to excite the nano-antenna. Based on this optimized waveguide excitation, the sensing mechanism is realized through measurable angular shifts in the far-field radiation pattern caused by refractive index perturbations in the MUT.

Compared with existing nanoantenna-based biosensors that primarily rely on resonance wavelength shifts or single-frequency angular responses, the proposed sensor demonstrates stable sensing performance over a finite operational bandwidth. In addition, the developed analytical model enables identification of all supported modes in the HPW, allowing optimal mode selection based on propagation characteristics, which is not typically addressed in related beam-steering sensing studies. The close agreement between theoretical predictions and full-wave simulations further validates the proposed design methodology. Moreover, the proposed biosensor achieves enhanced angular sensitivity compared with recent radiation-pattern-based biosensing approaches[30].

The remainder of this paper is organized as follows. Section 2 presents the theoretical formulation and the design procedure of the hybrid plasmonic waveguide and nano-antenna. Section 3 discusses the biosensing application and performance evaluation of the proposed nano-antenna. The key characteristics and comparative analysis of the biosensor are provided in Section 4. Finally, Section 5 concludes the paper.

Nano-Antenna Design Procedure

Hybrid Plasmonic Waveguide

The design of the proposed nano-antenna–based biosensor follows a structured and optimized procedure to achieve optimal performance. It begins with the development of a novel hybrid plasmonic waveguide. Hybrid Plasmonic Waveguides (HPWs) are a specialized class of optical waveguides that combine features of dielectric and plasmonic waveguides, enabling the efficient propagation of light waves[32–35]. These waveguides excel in enhancing light intensity, outperforming other conventional optical waveguides. Plasmonic waveguides use surface plasmon polaritons to confine light through the interaction between dielectric and metal surfaces, while dielectric waveguides utilize total internal reflection to propagate electromagnetic waves. Through the integration of these two distinctive waveguide types, HPWs have emerged as a novel waveguide category with the same characteristics. However, it's important to acknowledge that HPWs exhibit relatively high propagation losses, albeit demonstrating improvement compared to traditional waveguides.

We have designed a novel HPW featuring a rectangular cross-sectional geometry, purposed at introducing distinct HPW for nano-antenna application. Illustrated in Fig.1, our HPW structure comprises three distinct layers: a central layer composed of aluminum, flanked by adjacent layers of silicon dioxide and outermost silicon. Since the aluminum layer has a dielectric constant with a negative real part, it is expected that SPPs propagate along the aluminum-silicon dioxide interface. Additionally, it is anticipated that the higher dielectric constant of silicon compared to silicon dioxide confines the electric field within the silicon dioxide layer, which is a result of the principles of total internal reflection observed in dielectric waveguides. Additionally, SPPs propagate along the aluminum surface, further contributing to the presence of the electric field within the silicon dioxide layer. Utilizing the Rakic model[36], the dielectric constant of aluminum at the frequency of interest (450 THz) is $\varepsilon_{r_{Al}} = -60 + j27$. Furthermore, based on the models established by Malitson[37] and Green[38], the respective dielectric constants for silicon dioxide and silicon are $\varepsilon_{r_{SiO_2}} = 2.1$ and $\varepsilon_{r_{Si}} = 14.5 + j0.1$.

Theoretical Analysis of a Proposed Waveguide

The critical aspect of this design lies in ensuring that the proposed waveguide precisely generates the expected optical response. To validate the predicted behavior, a theoretical analysis is performed to confirm the performance of the proposed HPW. As plasmonic waves propagate within HPWs, the supported propagation mode is transverse magnetic (TM), indicating that the magnetic field component along the propagation direction is zero. Based on this assumption, the electric and magnetic field

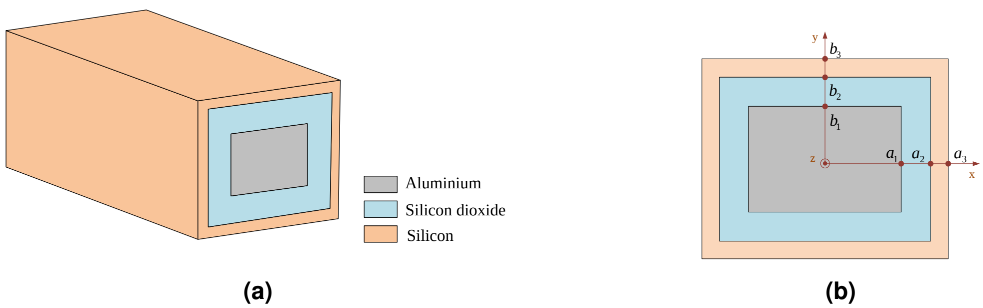

Figure 1. The schematic of the designed HPW. (a) 3D view. (b) 2D view. The width of Aluminum, silicon dioxide and silicon are $2a_1 = 130$ nm, $2a_2 = 180$ nm, and $2a_3 = 210$ nm, respectively. Also, the height of aluminum is $2b_1 = 90$ nm, and for silicon dioxide and silicon are $2b_2 = 140$ nm and $2b_3 = 170$ nm, respectively.

components are derived from Maxwell's equations. To determine the remaining field components in each layer, an appropriate closed-form expression for E_z is required. The longitudinal electric field E_z in each layer can be expressed in the conventional form as:

$$E_{1z} = \sum_n \sum_m A_n A_m' \cosh(k_{1nx}x)\cosh(k_{1my}y) \tag{1a}$$

$$E_{2z} = \sum_n \sum_m B_n B_m' \cosh(k_{2nx}x)\cosh(k_{2my}y) \tag{1b}$$

$$E_{3z} = \sum_n \sum_m C_n C_m' \cosh(k_{3nx}x)\cosh(k_{3my}y) \tag{1c}$$

$$E_{4z} = De^{-k_{4x}|x|}e^{-k_{4y}|y|} \tag{1d}$$

Here, the indices 1,2,3, and 4 correspond to aluminum, silicon dioxide, silicon, and free space, respectively. A,B,C, and D denote the field coefficients, while $k_i x$ and $k_i y$ represent the propagation constants in the x and y directions for each layer, respectively. The electric field in each layer is expressed as a summation of hyperbolic cosine (cosh) functions, which serve as the chosen basis functions for satisfying the field distribution across the multilayer structure. The cosh function is selected as the basis due to the even symmetry of the HPW. Each component of the electric and magnetic fields in every layer can be derived from equation (1). The relationships between the field coefficients of adjacent layers are obtained by applying the appropriate boundary conditions at each interface. However, considering all terms in the double summation introduces significant algebraic complexity. To simplify the formulation, only the first term of the summation in each layer is retained. Owing to the even symmetry of the waveguide, the boundary conditions are enforced at $x = a_1, a_2, a_3$ and $y = b_1, b_2, b_3$. Consequently, the five field components-E_x, E_y, E_z, H_x, and H_y-along with the six specified boundaries, yield a set of equations that can be categorized as follows:

$$[M]_{4\times4}[T]_{4\times1} = 0, \tag{2}$$

where $[T]$ represents the coefficient vector consisting of A, B, C, and D, and $[M]$ is a 4×4 matrix whose elements depend on the propagation constants in each layer. The matrix form can be expressed as:

$$\begin{bmatrix} m_{11} & m_{12} & 0 & 0 \\ 0 & m_{22} & m_{23} & 0 \\ 0 & 0 & m_{33} & m_{34} \\ 0 & m_{42} & m_{43} & 0 \end{bmatrix} \begin{bmatrix} A \\ B \\ C \\ D \end{bmatrix} = 0 \tag{3}$$

As a result of applying the boundary conditions, all components of the matrix $[M]$ are obtained as follows:

$$m_{11} = \cosh(k_{1x}a_1)\left(\frac{\sinh(2k_{1y}b_1)}{2k_{1y}} + b_1\right) \tag{4a}$$

$$m_{12} = -\cosh(k_{2x}a_1) \times \left(\frac{\sinh((k_{2y}+k_{1y})b_1)}{k_{2y}+k_{1y}} + \frac{\sinh((k_{2y}-k_{1y})b_1)}{k_{2y}-k_{1y}}\right) \tag{4b}$$

$$m_{22} = \cosh(k_{2x}a_2)\left(\frac{\sinh(2k_{2y}b_2)}{2k_{2y}} + b_2\right) \tag{4c}$$

$$m_{23} = -\cosh(k_{3x}a_2) \times \left(\frac{\sinh((k_{3y}+k_{2y})b_2)}{k_{3y}+k_{2y}} + \frac{\sinh((k_{3y}-k_{2y})b_2)}{k_{3y}-k_{2y}}\right) \tag{4d}$$

$$m_{33} = \cosh(k_{3x}a_3)\left(\frac{\sinh(2k_{3y}b_3)}{2k_{3y}} + b_3\right) \tag{4e}$$

$$m_{34} = -e^{-k_{4x}a_3} \times \left(\frac{2k_{4y}}{k_{4y}^2 - k_{3y}^2} - \frac{e^{-\left(k_{4y}+k_{3y}\right)b_3}}{k_{4y}+k_{3y}} - \frac{e^{-\left(k_{4y}-k_{3y}\right)b_3}}{k_{4y}-k_{3y}}\right) \tag{4f}$$

$$m_{42} = \cosh(k_{2y}b_2)\left(\frac{\sinh(2k_{2x}a_2)}{2k_{2x}} + a_2\right) \tag{4g}$$

$$m_{43} = -\cosh(k_{3y}b_2) \times \left(\frac{\sinh((k_{3x}+k_{2x})a_2)}{k_{3x}+k_{2x}} + \frac{\sinh((k_{3x}-k_{2x})a_2)}{k_{3x}-k_{2x}}\right) \tag{4h}$$

Equation (2) has a valid solution only when the determinant of the matrix $[M]$ equals zero. Accordingly, by setting $det([M]) = 0$, the dispersion relation of the HPW can be expressed as:

$$\begin{aligned} -e^{-k_{4x}a_3}\cosh(k_{1x}a_1)&\left(\frac{\sinh(2k_{1y}b_1)}{2k_{1y}} + b_1\right)\left(\frac{2k_{4y}}{k_{4y}^2 + k_{3y}^2} - \frac{e^{-(k_{4y}+k_{3y})b_3}}{k_{4y}+k_{3y}} - \frac{e^{-(k_{4y}-k_{3y})b_3}}{k_{4y}-k_{3y}}\right) \\ &\times\Bigg[-\cosh(k_{3y}a_2)\cosh(k_{2y}b_2)\left(\frac{\sinh((k_{3y}+k_{2y})b_2)}{k_{3y}+k_{2y}} + \frac{\sinh((k_{3y}-k_{2y})b_2)}{k_{3y}-k_{2y}}\right) \\ &\times\left(\frac{\sinh(2k_{2x}a_2)}{2k_{2x}} + a_2\right) + \cosh(k_{3y}b_2)\cosh(k_{2x}a_2)\left(\frac{\sinh((k_{3x}+k_{2x})a_2)}{k_{3x}+k_{2x}}\right. \\ &\left. + \frac{\sinh((k_{3x}-k_{2x})a_2)}{k_{3x}+k_{2x}}\right)\left(\frac{\sinh(2k_{2y}b_2)}{2k_{2y}} + b_2\right)\Bigg] = 0, \end{aligned} \tag{5}$$

here, k_ix and k_iy (i=1,2,3,4) are complex quantities. Since the dispersion equation admits multiple solutions for the propagation constant, an appropriate optimization method is required to identify the dominant solution. Accordingly, Genetic Algorithm (GA) is employed to solve the dispersion equation and determine the propagation constants for each layer. Based on the characteristics of the HPW and dielectric waveguides, only solutions with propagation constants within the range of $k_0 n_{Si} < Im(k_{ij}) < k_0 n_{Al}$ (i=1,2,3,4, and j=x,y,z) are considered. Under these conditions, the contribution of higher-order terms decays rapidly, and the first term becomes dominant in describing the field distribution of the fundamental mode. The GA implementation was configured with a population size of 100, using the stochastic uniform selection method, and the stopping criterion was set to a function tolerance of 1×10^{-6}. The mutation rate was set to 0.01, and the maximum number of generations was set to 2400.

Also, to evaluate the field distribution in each layer, the corresponding field coefficients must be calculated. By normalizing the coefficient of the aluminum layer to unity (A=1), the coefficients of the remaining layers can be obtained as follows:

$$B = -\frac{m_{11}}{m_{12}} \tag{6a}$$

$$C = \frac{m_{22}m_{11}}{m_{23}m_{12}} \tag{6b}$$

$$D = -\frac{m_{42}m_{22}m_{11}}{m_{43}m_{23}m_{12}} \tag{6c}$$

A full-wave electromagnetic simulation is employed to validate the results obtained from the theoretical analysis. Utilizing the comprehensive numerical analysis method within CST Studio Suite software, we investigated the properties of our proposed HPW using the obtained coefficients and full-wave software. Using the Finite Integration Technique (FIT), this software performed a thorough analysis of the HPWs' attributes. The normalized electric field distribution along the x-axis (E_x) at $y = 0$ is presented in Fig.2a for both the theoretical analysis and the FIT simulation. Likewise, Fig.2b depicts the normalized electric field distribution along the y-axis (E_y) at $x = 0$ for both approaches. The slight discrepancy between the theoretical and FIT results originates from the simplification adopted in the analytical model, where only the first term of the closed-form expression for equation 1 is considered. In contrast, the FIT method accounts for all effective factors influencing the field distribution. Despite this approximation, the theoretical analysis demonstrates strong agreement with the full-wave simulation, confirming the validity of the proposed model.

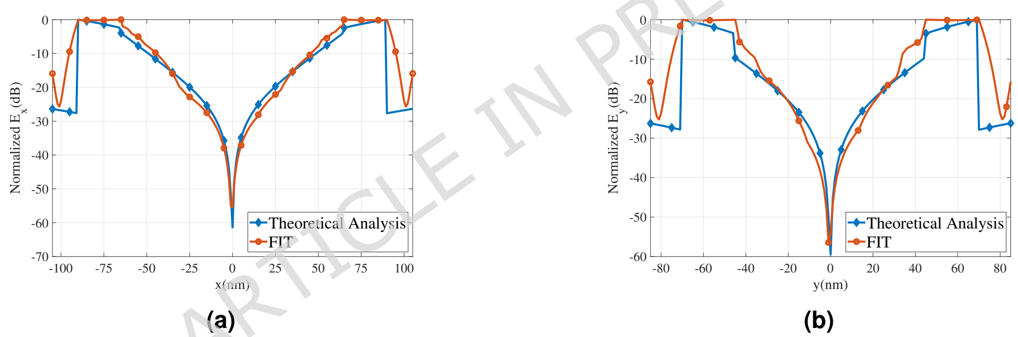

Figure 2. Comparison between the theoretical analysis and FIT: (a) Normalized E_x distribution along the x-axis at $y = 0$. (b) Normalized E_y distribution along the y-axis at $x = 0$.

In plasmonic waveguides, two fundamental parameters are the propagation length and the refractive index. The propagation length specifies the maximum distance over which the plasmonic wave can propagate efficiently within the waveguide. Meanwhile, the refractive index quantifies the ratio of the propagation constant in the HPW to that in free space. These parameters are depicted in Fig.3, which shows both the real part of the refractive index and the propagation length.

Rectangular Aperture Nano-Antenna

Leveraging the distinctive characteristics of the designed HPW, we developed a novel nano-antenna based on plasmonic waves. To design nano-antenna, the HPW served as the input port of the nano-antenna, while the output port was formed by expanding each layer of the HPW. Within this framework, plasmonic waves propagating through the HPW dispersed at the output port and radiated into the surrounding space. The resulting design is illustrated in Fig.4.

To comprehensively investigate the attributes of the devised rectangular aperture nano-antenna (RANA), we employed two distinct numerical simulation methods: the FIT and the Finite Element Method (FEM). These widely adopted simulation methods are facilitated by CST Microwave Studio and COMSOL Multiphysics, respectively. In the FIT simulations, waveguide port excitation was applied along with open (add space) boundary conditions, and the mesh refinement accuracy was set to 1×10^{-3}. In the FEM simulations, numeric port excitation was employed with perfectly matched layer (PML) boundary conditions. We meticulously assessed several key characteristics of the novel nano-antenna design through this dual method. First, we studied the reflection coefficient between the designed HPW and the radiating part of the RANA, employing both

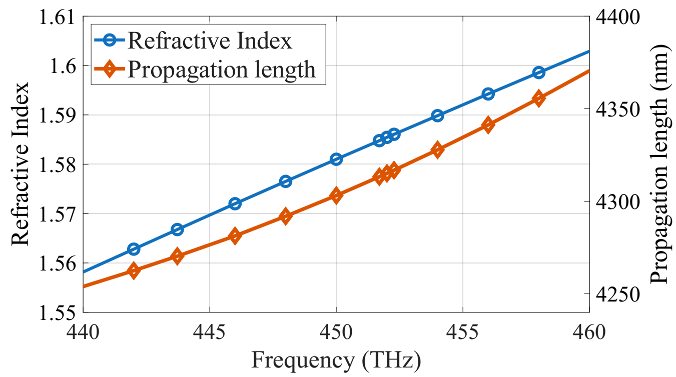

Figure 3. The real part of the effective refractive index and the propagation length of the proposed HPW

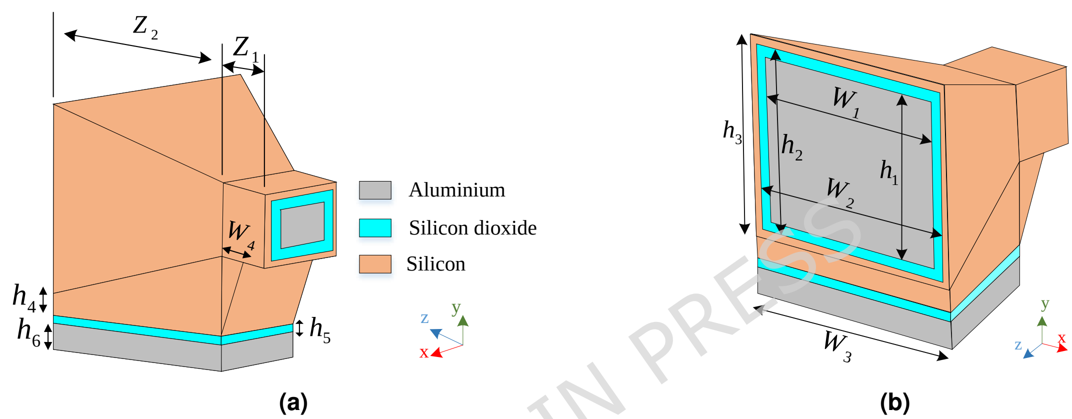

Figure 4. The scheme of the designed nano-antenna. (a) the 3D back view. (b) the 3D front view. The width of aluminum is $W_1 = 468$ nm at output port. Also, the width of the silicon dioxide and silicon layers is $W_2 = 518$ nm and $W_3 = 548$ nm, respectively. In addition, the height of the aluminum layer is $h_1 = 360$ nm, and the silicon dioxide and silicon layers are $h_2 = 410$ nm and $h_3 = 440$ nm, respectively. The length of the HPW is $Z_1 = 150$ nm. Also, the distance between the end of the HPW and the output port is $Z_2 = 399$ nm. Other relevant parameters include $W_4 = 75$ nm, $h_4 = 50$ nm, $h_5 = 20$ nm, and $h_6 = 60$ nm.

FIT and FEM techniques. As depicted in Fig.5, the reflection coefficient of the proposed RANA is obtained for both methods. Secondly, we conducted a detailed evaluation of the power flow radiation pattern, a key parameter critical to the nano-antenna's performance. Power flow represents the distribution of radiated power concentrated in a specific direction. Our comprehensive analysis utilized both simulation methods to thoroughly examine these characteristics. The quantification of power flow is expressed as:

$$\mathbf{S} = \mathbf{E} \times \mathbf{H}^*, \tag{7}$$

$$P = \int \mathbf{S}.dA, \tag{8}$$

where S, E, H, and P represent the Poynting vector, electric field, magnetic field, and power flow, respectively[39].

Fig.6 illustrates the power flow radiation pattern of the nano-antenna at 450 THz, analyzed using both the FIT and FEM methods, situated at the frequency band's center. The RANA exhibits a distinctive directional radiation pattern. The main lobe is oriented at 35 degrees from the z-axis, which corresponds to the front of the RANA. The directional pattern results from the distribution characteristics of surface plasmonic waves. This pattern forms the foundational basis for employing the RANA as a biosensor within the specified frequency band.

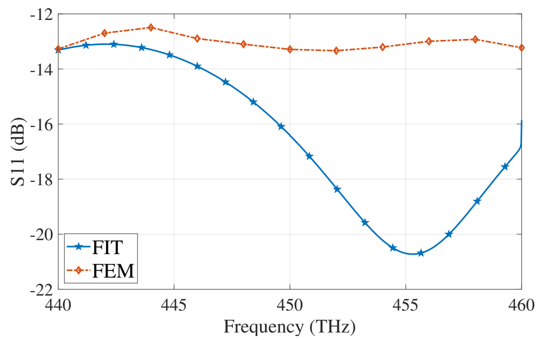

Figure 5. The obtained characteristic of the reflection coefficient by FIT and FEM methods, for designed RANA.

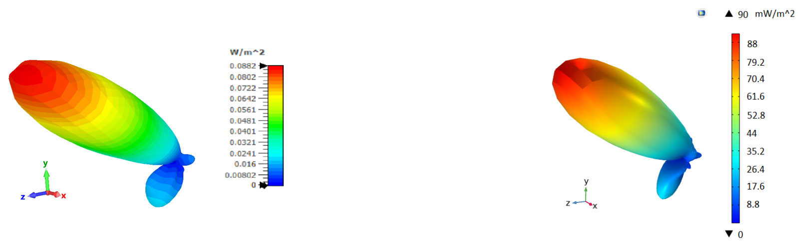

(a) (b)

Figure 6. Power flow distribution in the far-field region of the proposed nano-antenna. (a) FIT. (b) FEM.

Biosensor Based on Designed RANA

Protein as a Bio-material

The first step in the proposed biosensor design is the selection of an appropriate biomaterial. Proteins are chosen as the target biomaterial due to their extensive use in modern technologies, particularly in surface plasmon-based optical sensors. Proteins commonly serve as recognition or target elements for the selective detection of biological molecules, and their unique properties play a crucial role in cellular regeneration and repair. Consequently, monitoring protein characteristics is of significant importance. At optical frequencies in the visible and near-infrared regions, the dielectric constant of dry proteins typically lies within the range of 2 to 4. Semi-empirical methods based on molecular polarizability have been employed to estimate the static permittivity of dry proteins. These theoretical results are in good agreement with experimental measurements, indicating that the relative permittivity of dry proteins falls within the range of 2.5 to 3.5[40].

Biosensor Design

The inherent properties of the designed nano-antenna enable its potential use as a refractive index biosensor. The characteristics of the RANA inspired the decision to repurpose the rectangular aperture nano-antenna for biosensing applications. In this context, the radiation pattern emerges as a critical parameter, fundamental to the functionality of the biosensor. Illustrated in Fig.6, the proposed nano-antenna exhibits a directional radiation pattern. The primary objective of this study is to detect changes in the refractive index of bio-materials. Achieving this requires introducing the bio-material into the structure and evaluating its impact. Since plasmonic waves propagate within the silicon dioxide layer, this layer is selected for the insertion of the bio-material for analysis. To facilitate this, the HPW structure and its front part were divided into two distinct sections. One section was left unchanged, and the other was designed as the placement area for the material under test. The influence of the bio-material on the RANA's power flow radiation pattern is demonstrated by altering the surface plasmon polariton's propagation properties. Adjustments to the bio-layer's refractive index result in corresponding changes in the radiation pattern. The schematic representation of this RANA biosensor concept is depicted in Fig.7.

The difference in the refractive index of the protein alters the direction of the RANA's power flow radiation pattern. Specifically, we varied the refractive index of the dry protein within the range of 1.7 to 1.9. To evaluate the radiation pattern's sensitivity to these changes and establish it as a key output parameter for detecting the protein's refractive index, we systematically adjusted the protein's refractive index in increments of 0.029. For each increment, simulations of the structure were conducted to analyze its response following the insertion of the protein. Before examining the radiation pattern, it is crucial to evaluate the biosensor's return loss after the bio-layer is introduced. Fig.8a shows the return loss, which remains

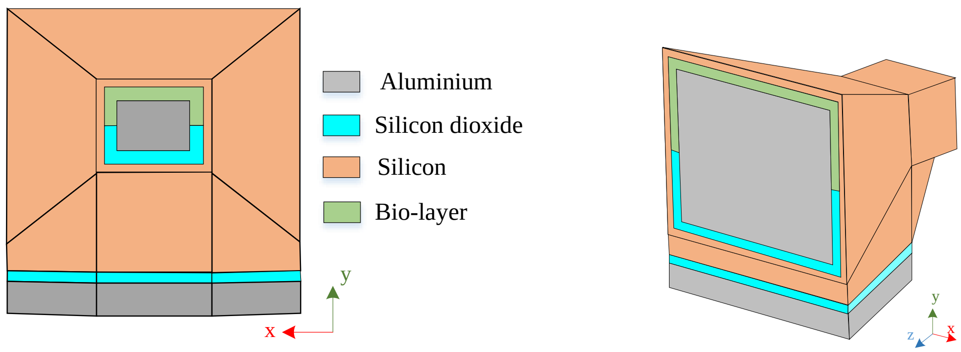

(a) **(b)**

Figure 7. The scheme of the proposed RANA biosensor. (a) the back view of the biosensor. (b) the 3D view.

below 10 dB across the entire frequency band, confirming the biosensor's suitability for this application.

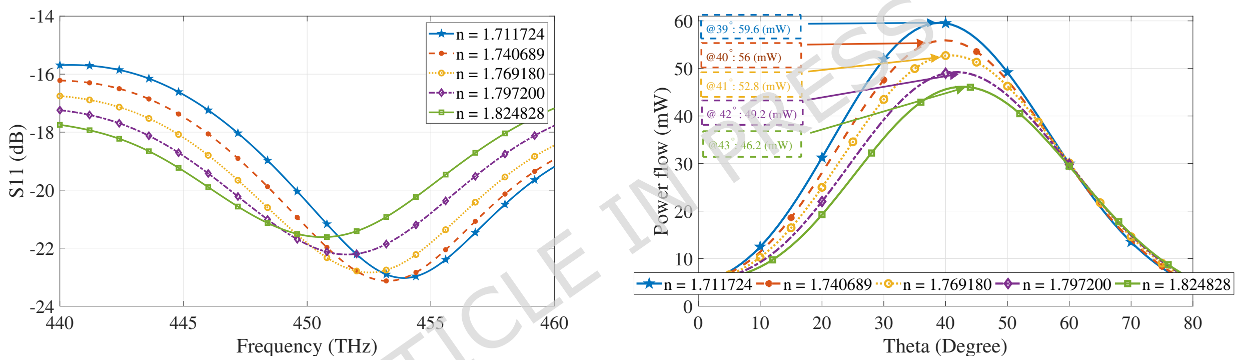

(a) **(b)**

Figure 8. (a) Return loss of the designed RANA biosensor. (b) Detecting the variation of bio-material's refractive index from directivity peak and beam direction at yz-plane.

As mentioned earlier, the radiation pattern of the RANA serves as the primary parameter in the biosensor's sensing process. To gain deeper insights into its operation, an analysis of the 2D radiation pattern in the yz-plane is particularly valuable. This plane corresponds to the peak of power flow and is defined at ϕ of 90 degrees, with θ representing the angle relative to the z-axis. Positive y-values correspond to positive θ angles, while negative y-values correspond to negative θ angles. Fig.8b illustrates the power flow of the RANA biosensor as a function of θ. The figure shows that as the refractive index of the bio-layer increases, the direction of the power flow's maximum peak shifts toward higher angles. For instance, when the protein's refractive index is 1.7117, the power flow reaches a maximum of 59.6 mW at 39 degrees. Increasing the refractive index (n) results in a reduction in the biosensor's power flow and a corresponding shift in beam direction to higher angles. At $n = 1.8248$, the power flow decreases to 46.2 mW, with the peak occurring at 43 degrees. Notably, in each step, a one-degree shift in the main beam direction can be experimentally detected using conventional far-field measurement techniques such as Fourier-plane (back focal plane) imaging, which can provide angular resolutions better than 1 degree[41]. This interplay between power flow and beam direction enhances the biosensor's ability to detect variations in the refractive index of the bio-material, thereby improving its diagnostic precision.

Properties of the Proposed Biosensor

This section presents properties of the proposed biosensor, emphasizing its operational principles and the interaction between plasmonic waves and the bio-material. The analysis focuses on key performance parameters, including refractive index sensitivity, operational bandwidth, and the definition of a figure of merit (FoM). These factors collectively determine the biosensor's effectiveness in detecting variations in the refractive index of the MUT.

Sensitivity

For a deeper investigation of the RANA biosensor's characteristics, an exploration of its sensitivity can be conducted using the power flow radiation pattern depicted in Fig.8b. The sensitivity of the biosensor can be defined as follows:

$$S = \frac{d\theta}{dn}. \tag{9}$$

This equation considers the peak power direction (θ) along with the bio-material's refractive index (n). As evident from the pattern, a 0.029 change in the bio-material's refractive index leads to a one-degree shift in the peak power direction. So, the sensitivity, which is the ratio of 1 and 0.029, reaches a value of 34.5° per refractive index unit (°/RIU). The total variation of 0.1131 in refractive index corresponds to a 4-degree shift in peak power direction and a 13.4 mW decrease in power. This underlines the biosensor's capacity for effectively detecting changes in refractive index of bio-material.

Bandwidth

To enhance the probability of detecting changes in the refractive index, we explored the biosensor's performance across different frequencies. By comparing data from various frequencies to the previously gathered information, we can refine the accuracy of refractive index detection. Thus, we examined the biosensor within a 2 percent bandwidth centered around 450 THz, spanning from 445.5 THz to 454.5 THz. The biosensor's behavior at these frequencies is illustrated in Fig.9a and Fig.9b. Notably, the biosensor's radiation pattern follows the same trend observed at the central frequency. Specifically, for a 0.1131 change in the refractive index, the peak power direction undergoes an approximate 4-degree shift, as depicted in Fig.9a. Moreover, at 454.5 THz, the RANA biosensor remains adept at detecting variations in the refractive index of bio-material. As demonstrated in 9b, peak beam direction and power flow fluctuate within the ranges of 37 to 41 degrees and 59.1 to 47.4 mW, respectively.

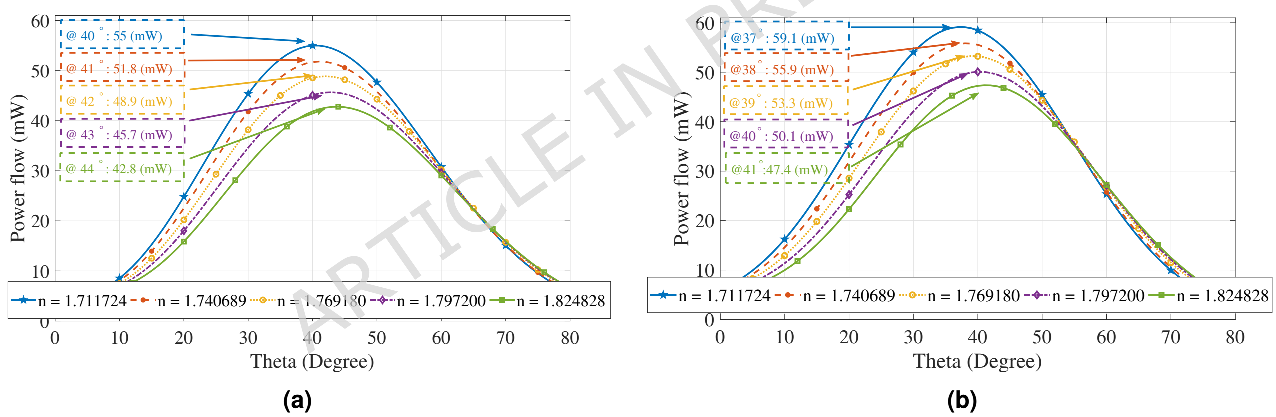

Figure 9. Operation of the designed RANA biosensor in the 2% bandwidth of the 450 THz. (a) 445.5 THz. (b) 454.5 THz.

Figure of Merit

Defining a comprehensive figure of merit (FOM) enables a more reliable comparison among different biosensors. In nano-antenna-based biosensors, key performance parameters include sensitivity, device size, operating bandwidth, and half-power beamwidth (HPBW). While sensitivity and HPBW are commonly used in conventional evaluations, biosensor size is crucial for on-chip integration, and broadband operation improves detection reliability by enabling sensing over multiple frequencies. Therefore, size and bandwidth are incorporated into the proposed FOM to provide a more complete performance assessment. During the design process, it is crucial to aim for a lower HPBW and size while striving for higher values of sensitivity and bandwidth. Therefore, we define the FOM using the following equation:

$$FOM = \frac{S}{HPBW} \times \frac{\Delta\lambda_{BW}}{L}, \tag{10}$$

where S $[°/RIU]$, $\Delta\lambda_{BW}$ $[\mu m]$, and L $[\mu m]$represent the sensitivity, frequency bandwidth, and maximum size of the biosensor, respectively. The unit of measurement for the FOM is RIU^{-1} (Refractive Index Unit). We investigated the figure of merit

(FOM) parameters for the proposed biosensor, which are derived from the radiation pattern of the nanoantenna. Previous studies have not focused on this radiation-pattern-based approach but have instead examined other parameters, such as reflection characteristics. Table **??** provides a comparison of recent works, highlighting the parameters and performance metrics introduced in each study.

Table 1. Comparison between the proposed biosensor and recent studies

References	Sensitivity ($\frac{\circ}{RIU}$)	HPBW (°)	$\Delta\lambda(\mu m)$	$L_{max}(\mu m)$	FOM
[14]	–	4.6	1.08	10.08	–
[30]	33	13.5	0	5.175	0
Our Work	34.5	37	0.013	0.792	0.0153

Fabrication Feasibility and Tolerance Analysis

Fabrication of the proposed nano-antenna can be achieved using high-resolution nanofabrication techniques such as electron-beam lithography (EBL), focused ion beam (FIB) milling, and standard thin-film deposition processes for silicon dioxide and silicon layers, which are widely employed for plasmonic nanostructure fabrication[43,44]. The fabrication feasibility steps of the proposed rectangular aperture nano-antenna (RANA) are illustrated in Fig.10. In the first step, the central aluminum layer is formed by patterning an aluminum film using lithography. In the subsequent steps, the silicon dioxide and silicon layers are sequentially deposited around the aluminum layer to complete the proposed multilayer structure. To evaluate fabrication feasibility, a dimensional tolerance of 5% was considered. Such variations may slightly affect the radiation characteristics, leading to small changes in the main beam direction, maximum power flow, and half-power beamwidth. Since the silicon dioxide and aluminum layers play a dominant role in hybrid plasmonic wave propagation, the key structural parameters shown in Figs.1 and 4 were examined under a 5% dimensional variation. The tolerance analysis results are summarized in Table 2, indicating that the corresponding deviation in the sensor output parameters remains below 8%.

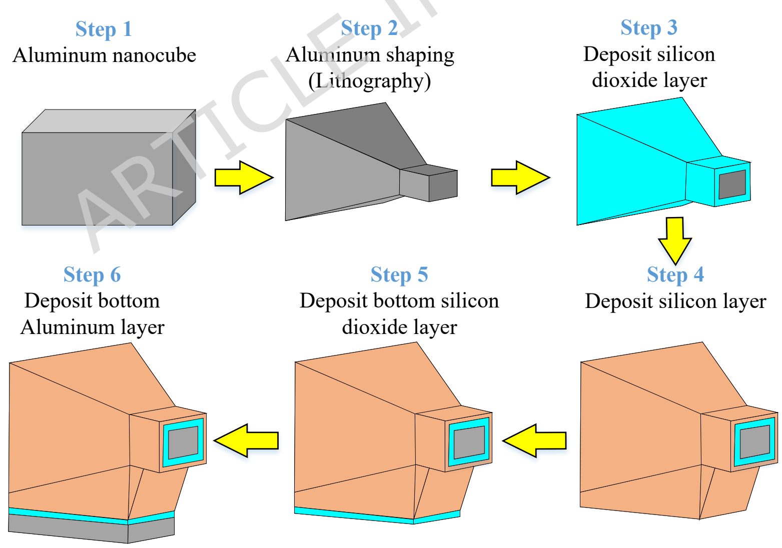

Figure 10. Fabrication feasibility steps of the proposed RANA structure.

Conclusion

In this paper, a novel plasmonic biosensor based on a hybrid plasmonic waveguide-fed rectangular aperture nano-antenna was proposed and analyzed for detecting refractive index variations in dry protein. The nano-antenna structure, composed of aluminum, silicon dioxide, and silicon layers, was designed to operate at 450 THz and exhibits a highly directional radiation pattern, which forms the basis of the sensing mechanism. A rigorous theoretical analysis was performed to derive

Table 2. Geometrical fabrication tolerances of the proposed nano-antenna structural parameters.

Parameter	Value (nm)	Main Beam Direction (°)	HPBW (°)	Power (mW)	Deviation (%)
W_1	468(-23.4/+23.4)	36/35	37.3/37.3	87.2/88	0.8-2.8
h_1	360(-18/+18)	38/32	38/36.4	81.5/81.4	2.7-8
Z_2	399(-19.95/+19.95)	38/32	37.5/36.5	81.1/81.3	1.3-8
$2a_1$	130(-6.5/+6.5)	36/35	37.3/37.4	86.7/88.5	0.8-2.8
$2b_1$	90 (-4.5/+4.5)	35/36	37.3/37.3	88.6/88.5	0.8-2.8
$W_2 - W_1$ [1]	25(-1.25/+1.25)	35/35	37.3/37.3	88.3/88.8	0-0.8
$h_2 - h_1$ [1]	25(-1.25/+1.25)	35/35	37.2/37.5	87.8/88.7	0-1.3

[1] Silicon dioxide layer size.

the dispersion relation of the hybrid plasmonic waveguide and to identify the dominant propagating mode using a genetic algorithm. The theoretical predictions were validated through full-wave numerical simulations, demonstrating excellent agreement. By exploiting radiation pattern characteristics such as beam direction and power flow, the proposed biosensor was shown to detect small refractive index variations of up to 0.029 in the dry protein. The results confirm that the proposed design achieves high sensitivity and accuracy compared with existing radiation-pattern-based biosensing approaches. Furthermore, the proposed biosensor maintains effective performance over a 2% bandwidth around the central frequency, enhancing its practical applicability. The combination of a comprehensive theoretical framework, directional nano-antenna design, and broadband operation makes the proposed biosensor a promising candidate for advanced biosensing applications.

References

1. Javaid, Zunaira, et al. "Reviewing advances in nanophotonic biosensors." Frontiers in Chemistry 12 (2024): 1449161.
2. Chadha, Utkarsh, et al. "Recent progress and growth in biosensors technology: A critical review." Journal of Industrial and Engineering Chemistry 109 (2022): 21-51.
3. Naresh, Varnakavi, and Nohyun Lee. "A review on biosensors and recent development of nanostructured materials-enabled biosensors." Sensors 21.4 (2021): 1109.
4. Zhou, Jie, Yue Wang, and Guo-Jun Zhang. "State-of-the-art strategies of surface plasmon resonance biosensors in clinical analysis: A comprehensive review." Coordination Chemistry Reviews 520 (2024): 216149..
5. Murugan, Divagar, et al. "Recent advances in grating coupled surface plasmon resonance technology." Advanced Optical Materials 12.34 (2024): 2401862.
6. Shekhar, Aman, and Sanjoy Mandal. "Z-domain Modeling and Performance Evaluation of Triple Optical Ring Resonator with embedded Bragg Gratings as Optical Filter and Biosensor." IEEE Sensors Journal (2025).
7. Shekhar, Aman, and Sanjoy Mandal. "Design and Analysis of Modified Double Ring Resonator With Embedded High Contrast Optical Bragg Grating as an Optical Filter and a Biosensor." IEEE Transactions on Nanotechnology (2025).
8. Rafi, Shah Ali, et al. "Optical based surface plasmon resonance sensor for the detection of the various kind of cancerous cell." Cell Biochemistry and Biophysics 83.1 (2025): 689-715.
9. Datta, Metali Rani, et al. "An Innovative Method for Cancer Cell Identification with Optimized Surface Plasmon Resonace in Photonic Crystal Fiber." 2025 International Conference on Quantum Photonics, Artificial Intelligence, and Networking (QPAIN). IEEE, 2025.
10. Rafsan, Ahmed Afif, et al. "Surface plasmon resonance–based biosensor for accurate and rapid detection of Mycobacterium tuberculosis." Microchimica Acta 192.12 (2025): 1-21.
11. Rafsan, Ahmed Afif, Md Imam Mahdi, and Md Rasedujjaman. "Ultra-sensitive Surface Plasmon Resonance Biosensor for Precise Malaria Detection." Sensing and Imaging 27.1 (2026): 84.
12. Emon, Wahiduzzaman, et al. "Hfo2-blue phosphorus/molybdenum disulfide hybrid structure-based surface plasmon optical refractometric sensor with multiple light source for rapid novel coronavirus detection." Optik 322 (2025): 172191.
13. Guo, Lanpeng, et al. "Electrochemical protein biosensors for disease marker detection: progress and opportunities." Microsystems and Nanoengineering 10.1 (2024): 65.
14. Kavitha, S., et al. "4×4 graphene nano-antenna array for plasmonic sensing applications." Discover Applied Sciences 6.9 (2024): 465.

15. Durmaz, Habibe. "A graphene-metal hybrid biosensor for SEIRA spectroscopy applications." Optics Communications 550 (2024): 130020.

16. Vigneshvar, S., et al. "Recent advances in biosensor technology for potential applications-an overview." Frontiers in bioengineering and biotechnology 4 (2016): 11.

17. Maier, Stefan A. Plasmonics: fundamentals and applications. Vol. 1. New York: springer, 2007.

18. Aftab, Muhammad, et al. "Surface plasmon excitation: theory, configurations, and applications." Plasmonics 19.4 (2024): 1701-1719.

19. Dey, Sumitra, et al. "Plasmonic nanoantenna optimization using characteristic mode analysis." IEEE Transactions on Antennas and Propagation 68.1 (2019): 43-53.

20. Singh, Ashish, et al. "A review on design, development and characterization of plasmonic nano-antenna for photonic applications." Journal of Optical Communications 45.s1 (2025): s2387-s2400.

21. Yi, Ke, et al. "Bowtie Nanoantenna LSPR Biosensor for Early Prediction of Preeclampsia." Biosensors 14.7 (2024): 317.

22. Bazgir, Maryam, et al. "The nano aperture in optical regime for bio-sensing, metasurface, and energy harvesting application: technical review." Sensors and Actuators A: Physical 359 (2023): 114495.

23. Srivastava, Akash, and Devendra Chack. "Plasmonic nanoantenna array-based sensor for air parameters monitoring purpose." Plasmonics (2024): 1-12.

24. Gandhi, Sakshi, and Suneet Kumar Awasthi. "Protein detection capabilities of photonic biosensor composed of 1D annular photonic crystal." Results in Optics 15 (2024): 100639.

25. Agrwal, Priyanka, and Ajay Kumar. "$In_{053}Ga_{047}$As-SOI-FinFET biosensor for ultra-sensitive point-of-care protein biomarker detection." Discover Applied Sciences (2025).

26. Khodadadi, Maryam, Najmeh Nozhat, and Seyyed Mohammad Mehdi Moshiri. "Theoretical analysis of a circular hybrid plasmonic waveguide to design a hybrid plasmonic nano-antenna." Scientific reports 10.1 (2020): 15122.

27. Khodadadi, Maryam, and Najmeh Nozhat. "Theoretical analysis of a super-mode waveguide and design of a complementary triangular hybrid plasmonic nano-antenna." IEEE journal of selected topics in quantum electronics 27.1 (2020): 1-10.

28. Mahmud, Russel Reza, et al. "Numerical Investigation of an Electrically Tunable Graphene–Based Perfect Metamaterial Absorber in the Terahertz Regime." Plasmonics 20.10 (2025): 8759-8770.

29. Wang, Bin, et al. "Design of aluminum bowtie nanoantenna array with geometrical control to tune LSPR from UV to near-IR for optical sensing." Plasmonics 15 (2020): 609-621.

30. Safaeian, Mohammad Reza, and Leila Yousefi. "A novel plasmonic bio-sensor operating based on optical beam steering." Journal of Lightwave Technology 40.1 (2022): 277-283.

31. Mahmud, Russel Reza, et al. "Dual-side polished SPR-PCF ultra-wide refractive index sensor with high amplitude sensitivity." Journal of Optics 27.2 (2025): 025101.

32. Oulton, Rupert F., et al. "A hybrid plasmonic waveguide for subwavelength confinement and long-range propagation." nature photonics 2.8 (2008): 496-500.

33. Kim, Jin Tae, et al. "Hybrid plasmonic waveguide for low-loss lightwave guiding." Optics express 18.3 (2010): 2808-2813.

34. Dai, Daoxin, and Sailing He. "Low-loss hybrid plasmonic waveguide with double low-index nano-slots." Optics express 18.17 (2010): 17958-17966.

35. Chen, Daru. "Cylindrical hybrid plasmonic waveguide for subwavelength confinement of light." Applied optics 49.36 (2010): 6868-6871.

36. Rakic, Aleksandar D. "Algorithm for the determination of intrinsic optical constants of metal films: application to aluminum." Applied optics 34.22 (1995): 4755-4767.

37. Malitson, Ian H. "Interspecimen comparison of the refractive index of fused silica." Josa 55.10 (1965): 1205-1209.

38. Green, Martin A. "Self-consistent optical parameters of intrinsic silicon at 300 K including temperature coefficients." Solar Energy Materials and Solar Cells 92.11 (2008): 1305-1310.

39. Balanis, Constantine A. Antenna theory: analysis and design. John wiley and sons, 2016.

40. Amin, Muhamed, and Jochen Kupper. "Variations in proteins dielectric constants." ChemistryOpen 9.6 (2020): 691-694.

41. Cueff, Sebastien, Lotfi Berguiga, and Hai Son Nguyen. "Fourier imaging for nanophotonics." Nanophotonics 13.6 (2024): 841-858.

42. Scalici, Marco, Samuele Scarpulla, and Patrizia Livreri. "A Novel Plasmonic Nanoantenna-Based Sensor with Graphene Tuning for Cancer Biomarker Detection." IEEE Sensors Journal (2025).

43. Nocerino, Valeria, et al. "Plasmonic nanosensors: design, fabrication, and applications in biomedicine." Chemosensors 10.5 (2022): 150.

44. Li, Hao, et al. "Study of SERS activity of different gold nanostructures prepared by electron beam lithography." Journal of Materials Science: Materials in Engineering 19.1 (2024): 44.

Author contributions statement

Mohammad AzimBeik conducted the conceptualization and design of the nanoantenna-based biosensor, developed the theoretical framework, performed all simulations and numerical analyses, interpreted the results, and prepared the manuscript. Professor Moradi and Professor Abdipour reviewed the methodology, verified the accuracy of the theoretical and numerical findings, and provided feedback to improve the clarity and technical quality of the manuscript.

Additional information

The authors declare no conflicts of interest related to this article.